1999-56

JOURNAL OF GEOPHYSICAL RESEARCH, VOL. 104, NO. A8, PAGES 17,005–17,019, AUGUST 1, 1999

Solar wind ionic charge states during the Ulysses pole-to-pole pass

Yuan-Kuen Ko,[1,2,3] George Gloeckler,[4,5] Christina M. S. Cohen,[6] and Antoinette B. Galvin[7]

Abstract. We analyze and compare the ionic charge composition data for different types of the solar wind (slow wind from equatorial regions, fast wind from low-latitude coronal hole and fast wind from both south and north polar coronal hole) which the Solar Wind Ion Composition Spectrometer (SWICS) on Ulysses observed during the pole-to-pole pass of its primary mission. The implications on the electron temperature, electron density, and ion outflow velocity from the corresponding solar wind source regions are also discussed. We find that the electron temperature in the source region of the slow solar wind is higher than that in the coronal hole. We also find a possible north-south asymmetry in the electron temperature that may be correlated to the north-south asymmetry in the solar wind speed found in the SWOOPS/Ulysses data. In particular, we make extensive discussions on the latitudinal variations in the polar coronal hole. On the basis of our data without clear constraints from other coronal observations, the preliminary result is that the electron density may be higher, or the heavy ion outflow velocities may be lower toward lower heliographic latitude.

1. Introduction

Ulysses was launched in October 1990 and after the Jupiter swingby in February 1992, the spacecraft was deflected out of the ecliptic plane over the south pole of the Sun where a maximum southern latitude of 80 deg was reached in September 1994. The pass from the south pole through the equatorial plane over the north pole of the Sun was rapid, with Ulysses reaching the highest northern latitude of 80 deg in July 1995. During its southward journey after the Jupiter swingby, the spacecraft began to observe a steady stream of high speed solar wind of 700 to 800 km/s from the south polar coronal hole after it reached a heliographic latitude of about 48 deg. Ulysses remained immersed in this high-speed stream as it moved northward until at approximately 25 deg south where it began to observe slow wind from the equatorial region alternating with fast wind from the coronal hole. Starting at 20 deg north Ulysses was once again immersed in a steady stream of high-speed solar wind, this time from the north polar coronal hole. Turning southward, it was not until ~30 deg north that observations of alternating slow and fast wind returned. *McComas et al.* [1998] have shown a polar plot of the solar wind proton speed observed by the solar wind plasma instrument (SWOOPS) on Ulysses since launch. It gives a clear structure of the observed solar wind in heliographic latitude during the minimum phase of this solar cycle. The data from the instruments onboard Ulysses are therefore unique in exploring the properties of the solar wind and the heliospheric structure for a large range of the heliographic latitude. In this paper, we analyze the ionic charge composition data in both the slow and fast solar wind measured by the Solar Wind Ion Composition Spectrometer (SWICS) [*Gloeckler et al.*, 1992] on Ulysses during its pole-to-pole fast scan. During this time, the spacecraft moves from 25 deg south to 20 deg north around its perihelion (1.34 AU). We also compare these data with the long-time averaged ionic charge states in the high-speed solar wind from the south and north polar coronal holes.

Under steady state condition, the solar wind ionic charge states are generally "frozen-in" within 5 solar radii of the Sun. The ions then stay in their frozen-in states in the solar wind flow through the interplanetary space. Therefore the observed in situ ionic charge states are a good probe to the physical properties in the inner solar corona where the ions' freezing-in process occurs. Different ionic charge composition in different types of the solar wind thus implies that the physical properties are different in these solar wind source regions.

In section 2, we describe the time periods selected representing different types of the solar wind during the pole-to-pole pass. The data analysis is discussed in section 3. In section 4, we show and compare the ionic charge composition data from these different types of the solar wind (specifically, polar coronal holes, low latitude coronal holes, and interstream "slow" wind). In section 5, we discuss the implications on the electron temperature, electron density and ion outflow velocity from the corresponding solar wind source regions based on these observed ionic charge states. In section 6, we give the summary of this study.

2. Data Selection

In February and March of 1995, Ulysses flew northward from 25 deg south to 20 deg north in heliographic latitude.

[1]Department of Atmospheric, Oceanic and Space Sciences, University of Michigan, Ann Arbor.
[2]Now at Harvard-Smithsonian Center for Astrophysics, Cambridge, Massachusetts.
[3]Also at Goddard Space Flight Center, Greenbelt, Maryland.
[4]Department of Physics, University of Maryland, College Park.
[5]Also at Department of Atmospheric, Oceanic and Space Sciences, University of Michigan, Ann Arbor.
[6]Space Radiation Laboratory, California Institute of Technology, Pasadena.
[7]Institute for the Study of Earth, Oceans, and Space, University of New Hampshire, Durham.

Paper number 1999JA900112.
0148-0227/99/1999JA900112$09.00

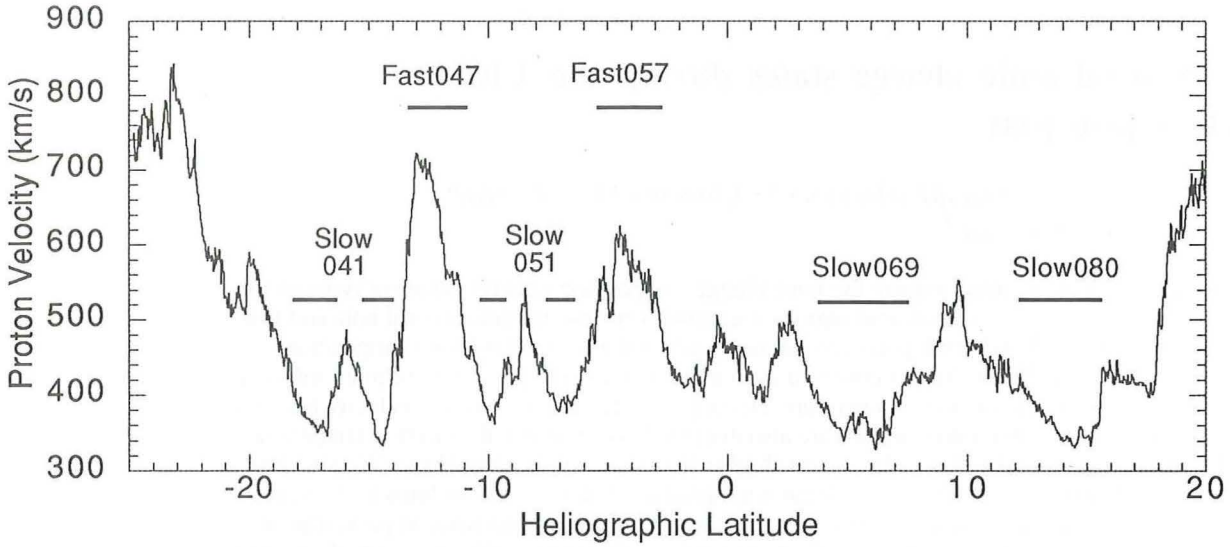

Figure 1. The solar wind proton speed measured by SWICS/Ulysses as a function of the in situ heliographic latitude during the Ulysses pole-to-pole fast scan in February and March 1995. The time periods selected for analysis of the slow and fast solar wind are also marked.

During this time, it observed periods of both slow and fast wind. Figure 1 shows the solar wind proton speed measured by SWICS/Ulysses as a function of in situ heliographic latitude during this pole-to-pole fast scan. The types of the solar wind and the time periods selected in this study are listed in Table 1 and explained below:

2.1. Slow Solar Wind

Four periods of the slow solar wind are selected for which v < 400 km/s. To make later reference easier, we denote them according to the starting day-of-year of the respective selection periods. They are Slow041, Slow051, Slow069, and Slow080. All of the above slow wind data are then summed up to represent the "averaged slow wind" denoted as Slow.

Note that the pole-to-pole fast scan covers approximately two solar rotations. Slow041 and Slow069 are separated in time by roughly one solar rotation. Slow051 and Slow080 are also separated by roughly one solar rotation. Interestingly, the interplanetary magnetic field (IMF) measurements from Ulysses showed that the magnetic polarity of the IMF is the same as the fast wind from the south polar coronal hole during the time when Slow041 and Slow069 were observed [*McComas et al.*, 1998]. Similarly, the magnetic polarity of the IMF is the same as the fast wind from the north polar coronal hole during the time when Slow051 and Slow080 were observed. If we assume the slow solar wind comes from the vicinity of the solar streamer, it is very likely that Slow041 and Slow069 correspond to the same streamer structure that has evolved over one solar rotation. Similarly, Slow051 and Slow080 correspond to the evolution of a second streamer structure.

2.2. Fast Solar Wind at Low Latitude

Two periods of the fast solar wind are selected for which v > 500 km/s. They are denoted as Fast047 and Fast057. These two periods of data are then summed to represent the averaged fast wind denoted as Fast. Note that during both periods, the

Table1. Time Periods Selected for Different Types of the Solar Wind

Wind Type	Denotation	Start Time[a]	End Time[a]
Slow, v<400 km/s	Slow041	1995/doy041/04:07:17 1995/doy045/00:24:54	1995/doy043/13:25:22 1995/doy046/16:38:54
	Slow051	1995/doy051/17:58:15 1995/doy055/07:30:27	1995/doy052/20:50:55 1995/doy056/22:23:41
	Slow069	1995/doy069/11:33:17	1995/doy074/03:59:38
	Slow080	1995/doy080/15:13:35	1995/doy084/16:42:28
Fast, v>500 km/s	Fast047	1995/doy047/11:00:46	1995/doy050/15:31:37
	Fast057	1995/doy057/23:44:00	1995/doy061/07:52:29
Fast, v>700 km/s	South	1994/doy001/00:00:00	1995/doy024/10:53:00
	North	1995/doy103/15:52:26	1996/doy213/23:59:59

[a]: In year/day-of-year/time(hour:min:s).

measured IMF has the same polarity as the fast wind from the south polar coronal hole. Mapping the solar wind back to the source region on the Sun, various solar magnetic field models have shown that both periods of the fast wind come from near the boundary of the south polar coronal hole [*Neugebauer et al.*, 1998]. In particular, the footpoints of the Fast057 data lie along the equatorial extension of the south polar coronal hole. On the other hand, *Woo and Habbal* [1997] suggested from the Ulysses radio occultation measurements that the fast wind at low latitude can actually be attributed to the ray-like ("plume") structures. These structures fill the space between the coronal hole boundary and the stalks of the streamers at large heliospheric distance and overlie the streamer structure close to the Sun. This would suggest that the source region for these "in-ecliptic" fast wind may be at much lower latitude on the Sun than previous models suggested.

To compare the above charge composition data with those from the polar coronal holes, we also extract the fast solar wind data when Ulysses was at high south and north heliographic latitudes.

2.3. Fast Solar Wind From the South Polar Coronal Hole

About 388.5 days of raw data are extracted which cover heliographic latitudes from 48 degrees south to 80 degrees south and back to 30 degrees south for which v > 700 km/s. We denote this data as South.

2.4. Fast Solar Wind From the North Polar Coronal Hole

About 474 days of raw data are extracted which cover heliographic latitudes from 30 degrees north to 80 deg north and back to 30 deg north for which v > 700 km/s. We denote this data as North.

Note that isolated periods of high-speed solar wind associated with coronal mass ejections (CMEs) were detected during the time when Ulysses was immersed in the fast streams from the south polar coronal hole. Also there is no CME detected during the pole-to-pole fast scan and in our North data [*Phillips et al.*, 1995; *Gosling et al.*, 1998]. The charge composition of such transient flows when originating from the in-ecliptic regions has been shown to have more abundant higher charge states than the fast wind from the coronal hole related regions, occasionally with the co-existence of exceptionally low charge states. However, the CME-associated solar wind charge states at higher latitudes are very similar to those from the polar coronal hole (see review by *Galvin* [1997]). In our South data, we do not exclude such CME-associated fast wind data. Since our selected data are overwhelmed by the polar coronal hole related fast wind, the charge composition data analyzed here should not be affected by the few CME-associated events.

3. Data Analysis

The pulse height analysis data (PHA data) were extracted from the Experiment Data Records (EDRs) processed at the University of Maryland. Mass (M) and mass-per-charge (M/Q) values were determined for each event from these data. For events falling within several "ion boxes" (as defined by their M/Q and mass boundaries given in Table 2), the events were binned in the M/Q-M space [see *Cohen*, 1995]. The data were then converted into ion fluxes by correcting for event priorities, instrument efficiency and duty cycle. The ranges of M/Q and M of the ion boxes for the "target ions" in our study are listed in Table 2. The ions (thus the range of M/Q) considered in the 2-D Gaussian fit (see below) for some ion boxes are different between the fast and slow wind, because we expect more abundant lower charge states in the fast wind than in the slow wind. Note that C and O boxes are only different in the defined range of mass. Although they are used to derive the ionic fractions of C and O ions respectively, the fitting results for both boxes agree to better than 5%. Figure 2 gives an example of the 3-D plot (ion fluxes in the M/Q-M space) which is for the "O box" of the North data. The major peak is the O^{+6} ion. The contributions from C^{+4}, C^{+5}, and C^{+6} ions are also obvious.

For each ion box, we fit the data with a number of 2-D Gaussians each of which corresponds to one particular ion believed to contribute to the flux in this ion box (Table 2). Each 2-D Gaussian (i.e., ion) is characterized by five parameters: its volume in the M/Q-M space, its M/Q, the full-width-half-maximum (FWHM) of M/Q, its mass and the FWHM of mass. The best-fit parameter values are calculated by using a least squares fit technique to fit the sum of the Gaussians to the ion flux matrix in the ion box. The ionic fractions for a given element are then calculated from the volumes of all best-fit 2-D Gaussians corresponding to this element. The full description of this 2-D Gaussian fitting technique is contained by *Cohen* [1995].

The instrument response calculated according to the calibration data shows that the FWHM of M/Q is generally around 6% of the M/Q and the FWHM of mass is generally around 30% of the mass [*Cohen*, 1995]. Thus the data distribution along the M/Q axis is narrow and well defined, but the distribution along the mass axis is very broad, as can be seen in Figure 2. From the multi-Gaussian fit, we find that the resulting best fit M/Q values and their FWHMs are usually very reasonable compared with the predicted instrument response as

Table 2. Ions and Boundaries of Selected Ion Boxes

Ion Box	Target Ions	Ions in 2-D Gaussian Fit	Range of M/Q	Range of M
C	C^{+4}-C^{+6}	C^{+4}-C^{+6}, N^{+5}-N^{+7}, O^{+6}-O^{+8}, Ne^{+8}	1.8-3.2	8.0-18.0
O	O^{+6}-O^{+8}	C^{+4}-C^{+6}, N^{+5}-N^{+7}, O^{+6}-O^{+8}, Ne^{+8}	1.8-3.2	9.0-20.0
Si Slow	Si^{+7}-Si^{+12}	Si^{+7}-Si^{+12}, Mg^{+7}-Mg^{+10}, S^{+8}-S^{+14}	2.0-4.1	24.0-36.0
Si Fast	Si^{+6}-Si^{+12}	Si^{+6}-Si^{+12}, Mg^{+6}-Mg^{+10}, S^{+7}-S^{+12}	2.2-4.9	24.0-36.0
Fe Slow	Fe^{+7}-Fe^{+16}	Fe^{+7}-Fe^{+16}, Ca^{+10}-Ca^{+11}	3.2-8.4	40.0-70.0
Fe Fast	Fe^{+7}-Fe^{+15}	Fe^{+7}-Fe^{+15}, Ca^{+8}-Ca^{+11}	3.2-8.4	40.0-70.0

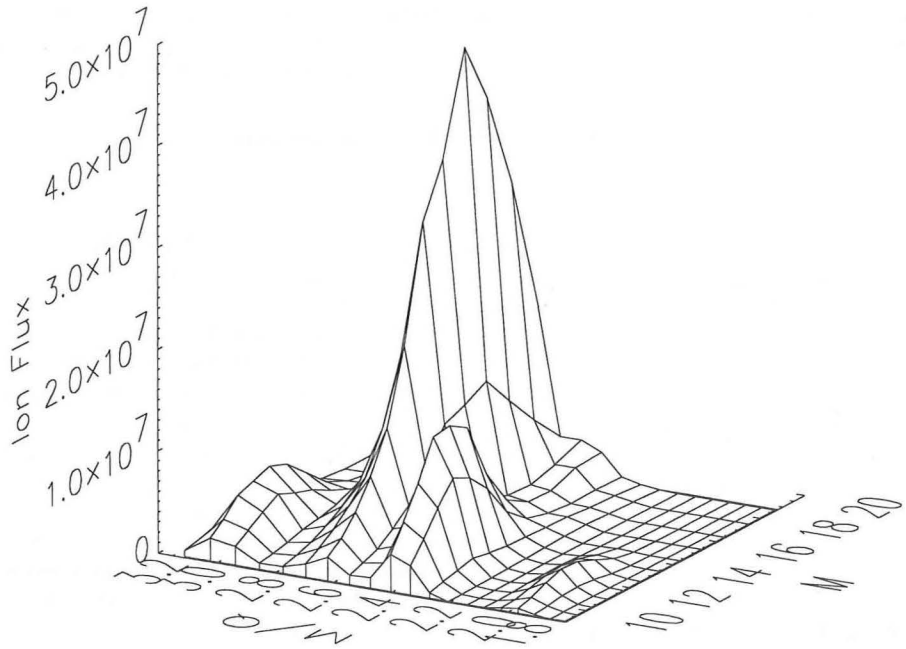

Figure 2. The pulse height analysis data of the O box in the M/Q-M space for the fast wind from the north polar coronal hole. The O^{+6} and C^{+4-+6} peaks can be clearly seen.

the peaks are well defined. The best fit mass values and their FWHMs, however, are in many cases very different from the predicted instrument response and their mass values are often different for ions of the same element which can be as large as 20%. This is due to the poorer resolution in the M space. Therefore we choose to fix the mass and the FWHM in mass at the predicted instrument response values in the fitting procedure. In this way, we make sure these values do not result in questionable numbers. We also limit the variation in the FWHM of M/Q to within +/- 1.6% of the predicted M/Q instrument response.

It is realized that there is no unique best fit result for this multi-Gaussian fitting of the PHA data. The result of the fit usually depends on the algorithm in the fitting procedure. This is due to the effect of ion mixing (i.e., the "spillover" from one ion species into the area of a neighboring species in the M/Q-M space), which is inherent in the PHA data. The difference in the fitting results between various fitting procedures depends on the extent of this ion-mixing effect in the ion box. For example, for C and O ions, there are not many ions in the vicinity of their M/Q-M area, they can be separated more accurately than the ions in the Si box. Within one given ion box, there are ions that are harder to separate than others. There is no easy objective judgment on which fitting procedure is the most accurate. For each ion box of each type of the solar wind, at least two fitting procedures are used, among one of them is the 'standard' fit described in the previous paragraph which is chosen to be our best fit result. The other frequently used procedure is to fix the mass at its predicted instrument response value but allow its FWHM to vary during the fit. The difference between the resulting volumes from these fitting procedures for a given ion is taken to be the initial error of the fit. This error implicitly reflects the effect of the ion-mixing problem. The final error for the volume is then the larger of this error and that from the multi-Gaussian fit, with a minimum cap of 10%. The error for the ionic fraction is subsequently calculated from the errors of these volumes corresponding to the same element by propagation of errors. Figure 3 gives examples of the Gaussian fit for the North data. Figure 3a shows the fit in the M/Q-space of the O box at an M "slice" (i.e., a subrange of M values) which contains the mass of oxygen (M=16). Figure 3b shows the fit in the M space of the O box at an M/Q slice, which contains the O^{+6} ion (M/Q=2.68). Figures 3c and 3d are similar to Figures 3a and 3b but are for the Si^{+9} ion in the Si box (M/Q=3.15, M= 28). The contribution from each element in the ion box is also plotted. We can see that the fits are generally pretty good. The ion mixing is a more serious problem in the Si box since there are many ions of Si, S, and Mg with their M/Q values close to one another.

4. Results

We compare the ionic charge composition from different types of the solar wind (the north polar hole, the south polar hole, low-latitude coronal holes, and interstream slow wind). We start the comparison in the context of the freezing-in temperatures. We will discuss in the next section how the difference in the ionic charge states infers the difference in the physical conditions between respective solar wind source regions. The freezing-in temperature of a given observed ionic ratio is defined as the electron temperature at which the abundance ratio of two neighboring charge states in ionization equilibrium is the same as the observed ratio. In ionization equilibrium, the abundance ratio of two neighboring charge states is fixed to the ratio of their ionization and recombination rates which are a function of the electron temperature. The higher the ratio of y_{i+1}/y_i (where y_i is the ionic fraction of charge $+i$), the higher the temperature [e.g., see *Arnaud and Rothenflug*, 1985]. In other words, the ionic charge composition in ionization equilibrium move toward higher charge states as the electron temperature increases.

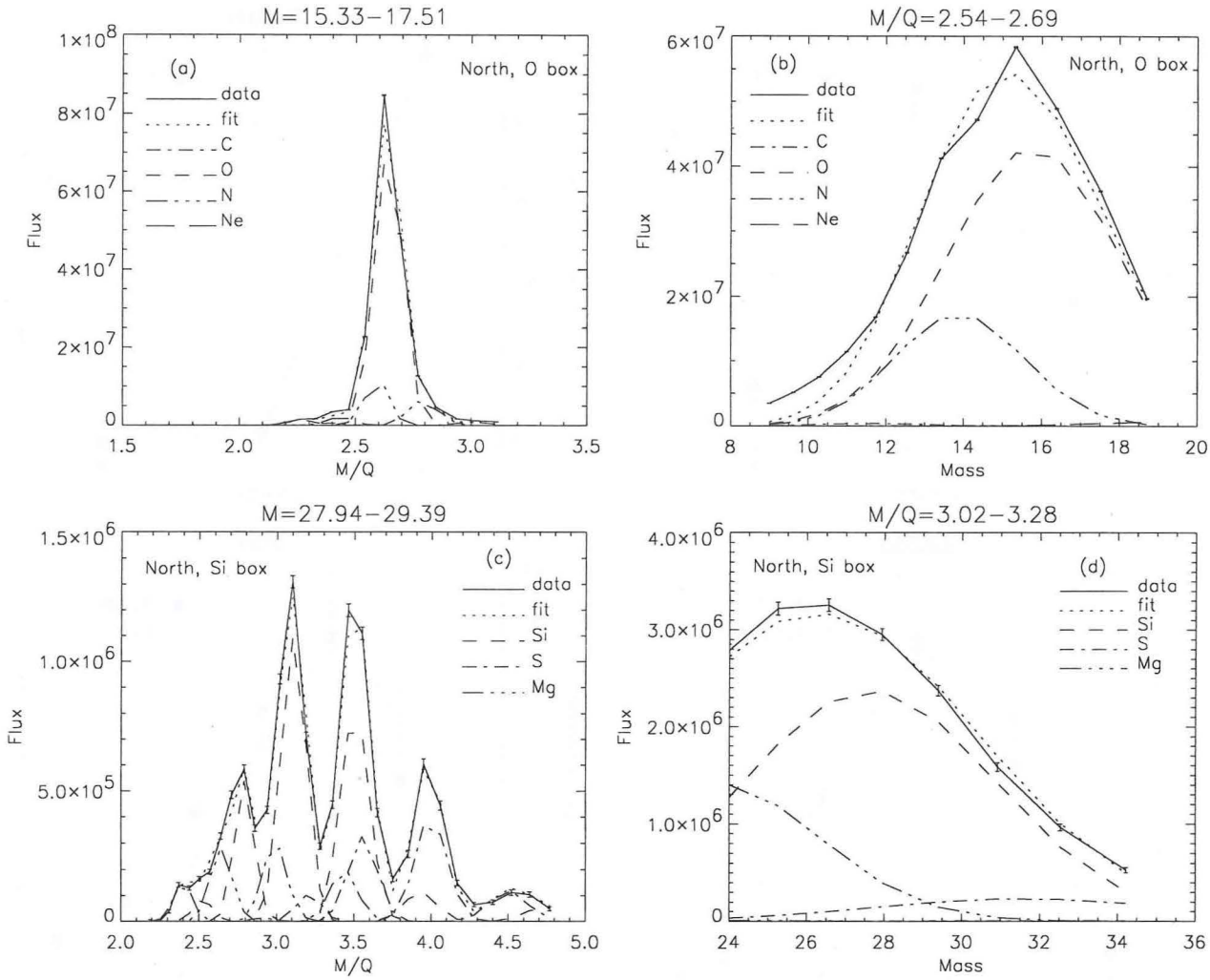

Figure 3. Examples of the 2-D Gaussian fit for the North data: (a) the fit in the M/Q-space of the O box at an M slice which contains the mass of oxygen (M=16); (b) the fit in the M-space of the O box at an M/Q slice which contains the O^{+6} ion (M/Q=2.68); (c) and (d) are similar to Figures 3a and 3b but are for the Si^{+9} ion in the Si box (M/Q=3.15, M= 28). The contribution from each element in the ion box is also plotted.

We choose the charge composition data from South as reference. Figure 4 compares the charge composition of C, O, Si, and Fe between South and North, Figure 5 compares the charge composition of C, O, Si, and Fe between South and Fast, and Figure 6 compares the charge composition of C, O, Si, and Fe between South and Slow. These comparisons show the following:

1. The freezing-in temperatures are slightly lower for North than that for South. This is inferred by the result that the lower charge states (e.g., Fe^{+8} - Fe^{+10}) for North are more abundant and the higher charge states (e.g., Fe^{+11} - Fe^{+14}) are less abundant than those for South. This is true for all four elements shown here.

2. The freezing-in temperatures of C and O ions are higher for Fast than those for South, but the freezing-in temperatures of Si and Fe ions are lower for Fast than those for South.

3. In the slow wind, the freezing-in temperatures are obviously higher for all elements. For example, the O^{+7}/O^{+6} ratio in Figure 6 corresponds to a freezing-in temperature of 1.75 x 10^6 K for Slow and 1.17 x 10^6 K for South. Note that these freezing-in temperatures are calculated explicitly from the ionization and recombination rates (the references are listed in section 5.3) instead of using the tables of *Arnaud and Rothenflug* [1985]. We note that the charge states from the south polar coronal hole can be roughly fitted by one electron temperature [*Geiss et al.*, 1995]. This is not the case for Si and Fe ions in the slow wind (see also *von Steiger* [1998]).

We also compare the frozen-in ionic charge composition from the same type of the solar wind but from different time periods. Figure 7 compares the charge composition of C, O, Si, and Fe between Fast047 and Fast057. It shows that the C and O ions from Fast057 freeze-in at higher temperature than Fast047, but the charge composition for Si and Fe ions are almost the same. Because of the lower statistics of these Si and Fe data, it is not clear that if the physical properties in these two solar wind source regions (at least at where these ions freeze-in) are very similar, or the apparent difference in the charge states of C and O does imply different properties in these source regions of the fast wind. Note that the average velocity during the period for Fast047 is higher than that for Fast057. Figure 8 compares the charge composition of C, O, Si, and Fe between Slow041, Slow051, Slow069, and Slow080. It shows that, not surprisingly, the charge states from different regions and time are far from similar. Thus the

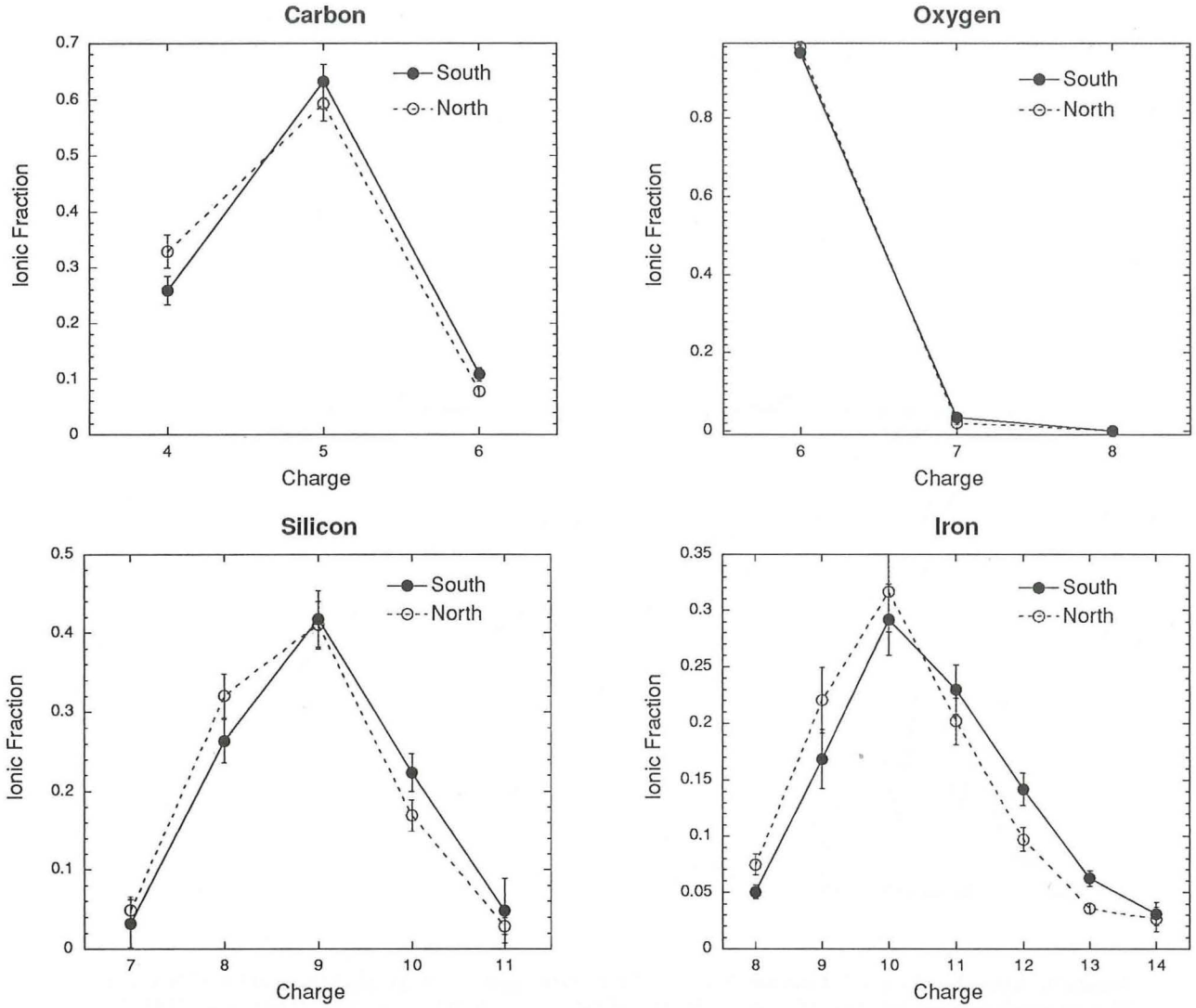

Figure 4. The C, O, Si, and Fe charge compositions of the fast solar wind from the north polar coronal hole (dashed curve) compared with those from the south polar coronal hole (solid curve).

average of the four (i.e., the Slow data) can only represent a typical slow wind and cannot correspond to a specific structure in the source region. It is suspected that the coronal properties at which the slow solar wind ions freeze-in may even vary significantly within timescales in which these individual slow wind data are accumulated. However, the freezing-in temperatures of these four slow wind periods shows a systematic difference. Figure 9 shows the freezing-in temperatures for C and Si ions. It is obvious that for C ions, T_f(Slow041) < T_f(Slow051) < T_f(Slow069) < T_f(Slow080). For Si ions, it seems that T_f(Slow051) < T_f(Slow041) < T_f(Slow069) < T_f(Slow080). As mentioned above, these four periods of the slow wind may correspond to two different streamer structures (041/069 versus 051/080) in two solar rotations (041 versus 069 and 051 versus 080). Therefore the in situ charge composition data can be used with other remote sensing observations to understand the dynamic behavior of the physical properties in the slow wind source regions.

5. Discussion

We have shown that the freezing-in temperatures of C/O ions is such that T_f(North) < T_f(South) < T_f(Fast) < T_f(Slow) and the freezing-in temperatures of Si/Fe ions is such that T_f(Fast) < T_f(North) < T_f(South) < T_f(Slow). This difference in the freezing-in temperatures, i.e., the ionic charge composition, directly reflects the difference in the physical properties, namely the electron temperature, the electron density and the ion outflow velocities in the freezing-in regions of these ions. We stress that the difference in the freezing-in temperatures does not necessarily infer the difference in only the electron temperature. Note that existence of nonthermal tail in the velocity distribution of coronal electrons can also affect the inference of coronal properties from the observed charge states [*Owocki and Scudder*, 1983; *Ko et al.*, 1996; *Esser et al.*, 1998; *Owocki and Ko,* 1999]. In this paper, we limit our discussion assuming the velocity distribution of coronal electrons is Maxwellian.

Consider a solar wind ion outflow where the ions of various ionization stages undergo constant ionization and recombination with the neighboring charge states through interaction with the electrons. In a steady state and assuming all ions of the same species flow at the same velocity u and only in the radial direction, the evolution of the ionic abundance of charge state i along the flow is [*Hundhausen et al.*, 1968]:

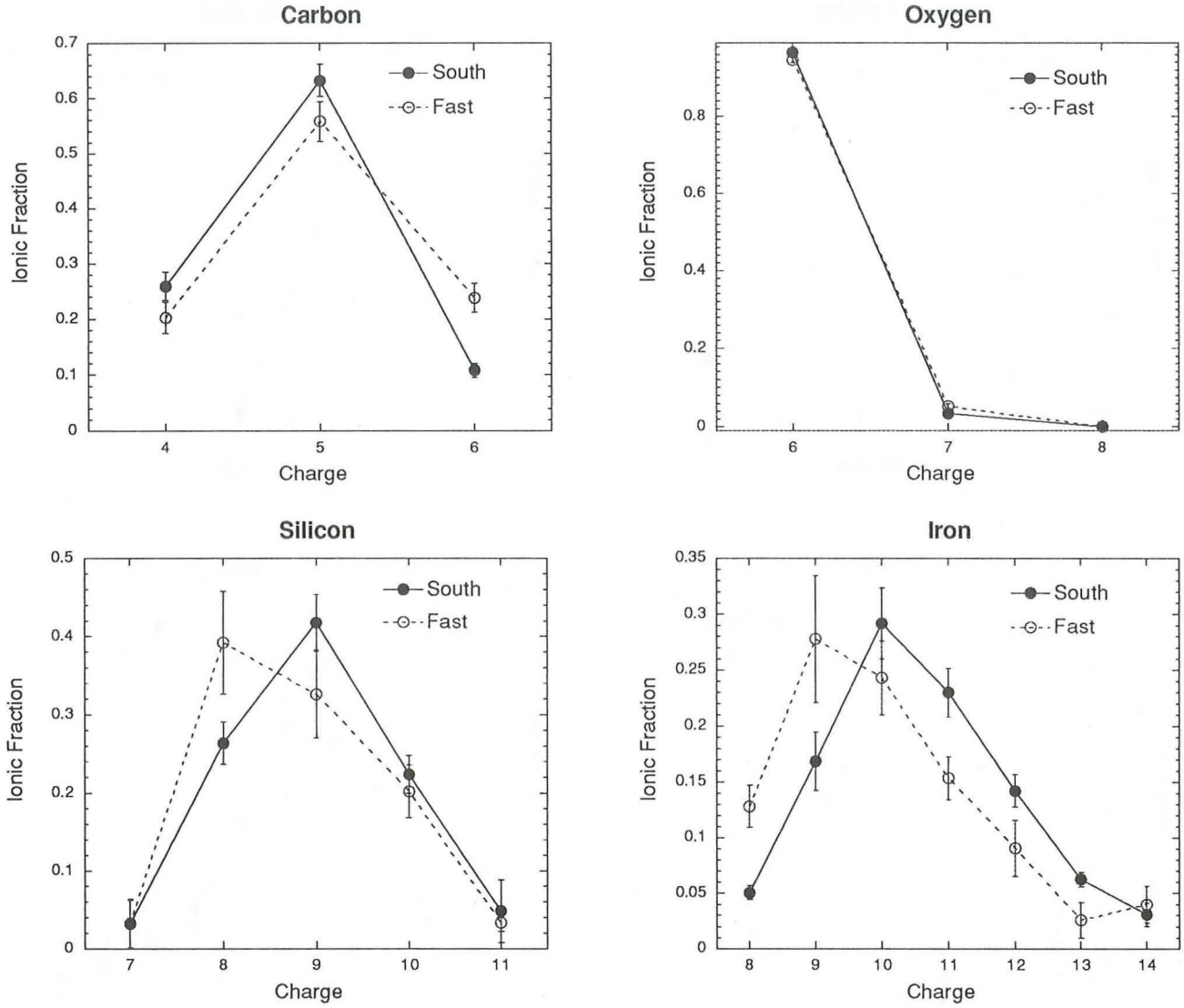

Figure 5. The C, O, Si, and Fe charge compositions of the Fast data (dashed curve) compared with those from the South data (solid curve).

$$u\frac{\partial y_i}{\partial r} = n_e(y_{i-1}C_{i-1} - y_i(C_i + R_i) + y_{i+1}R_{i+1}) \qquad (1)$$

where $y_i \equiv n_i / \sum_{i=0}^{i=Z} n_i$ is the ionic fraction of the ion with charge $+i$ of an element with atomic number Z, n_e is the electron density, u is the ion outflow velocity. The dependence of the freezing-in process on the electron temperature T_e lies in the rate coefficients C_i and R_i, where C_i is the total ionization rate (including collisional ionization and autoionization) from charge state i to $i+1$ and R_i is the total recombination rate (including radiative recombination and dielectronic recombination) from charge state i to $i-1$. Thus the evolution of the solar wind ionic charge states with heliocentric height depends on three physical quantities in the solar corona where the ions freeze-in: the electron temperature, the electron density and the ion outflow velocity. The freezing-in process occurs in the region where the expansion timescale

$$t_{exp} \equiv \left| \frac{u}{n_e}\frac{\partial n_e}{\partial r} \right|^{-1} \qquad (2)$$

is comparable to the ionization/recombination timescale:

$$t_{ion} \equiv \frac{1}{n_e(C_i + R_i)}. \qquad (3)$$

The charge states are in ionization equilibrium when $t_{exp} >> t_{ion}$ and are frozen-in when $t_{exp} << t_{ion}$, i.e. when

$$\frac{n_e}{u}(C_i + R_i)\left| \frac{1}{n_e}\frac{\partial n_e}{\partial r} \right|^{-1} << 1. \qquad (4)$$

Figure 10 shows the changes in the frozen-in ionic charge states for C and Fe ions responding to the change in either T_e, n_e, or u. As a "base model", we adopt a set of ($T_e(r)$, $n_e(r)$, $u(r)$) profiles which are among those that best fit the observed ionic charge state data for the fast solar wind from the south polar coronal hole during the first south polar pass of Ulysses [*Ko et al.*, 1997]. Note that the electron temperature profile has a local maximum in the freezing-in region. Here we assume the electron temperature profiles are similar in all fast wind source regions. We then calculate the frozen-in ionic charge states, according to equation (1), when (1) the electron temperature is 1.2 times higher, (2) the electron density is 2 times higher, or (3) the ion outflow velocity is 2 times higher, while other two parameters are kept the same. We choose

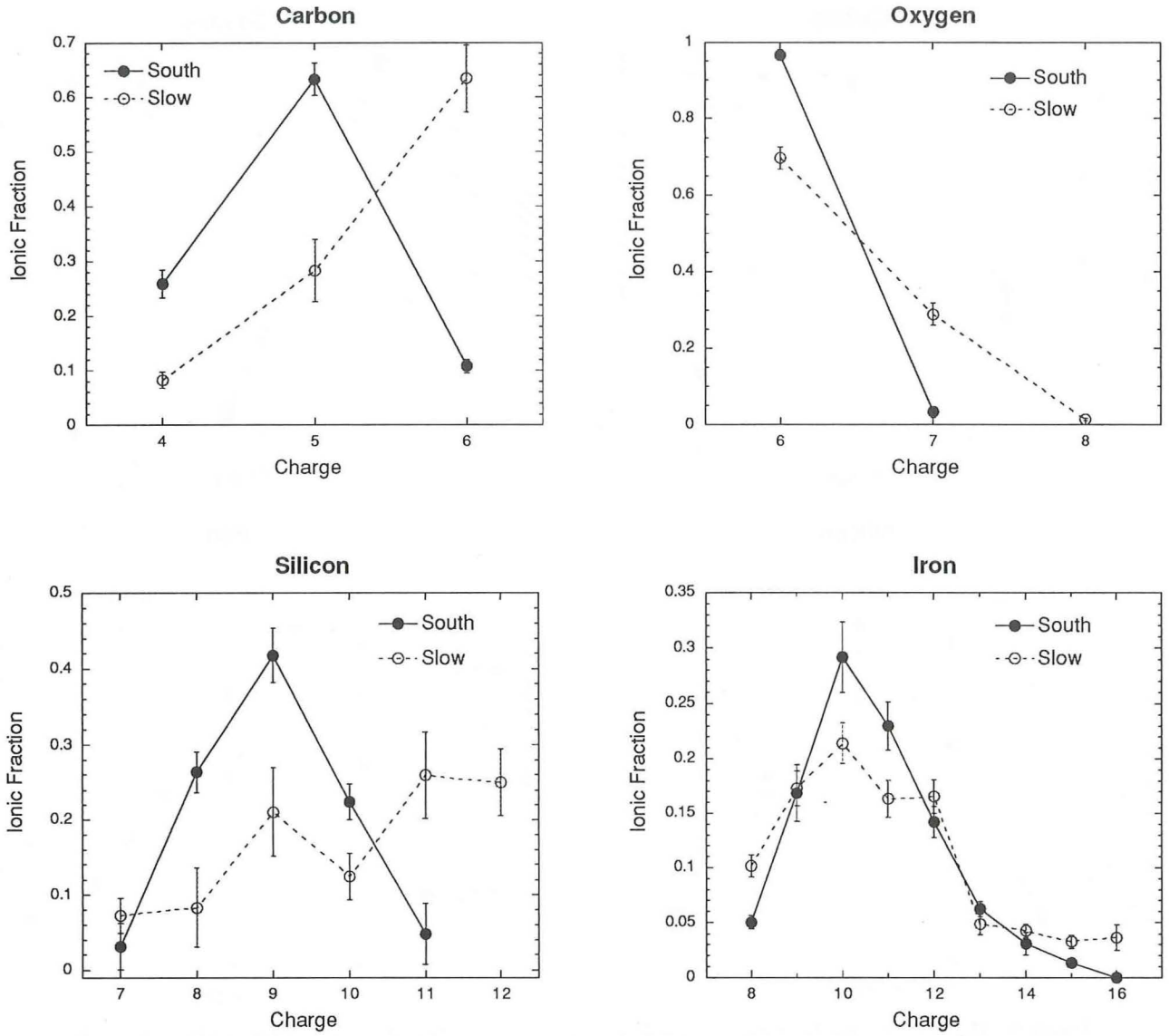

Figure 6. The C, O, Si, and Fe charge compositions of the slow solar wind from the equatorial region (dashed curve) compared with those of the fast solar wind from the South data (solid curve).

carbon and iron ions to illustrate the difference in the change in the charge composition when the ions are freezing-in before (carbon) or after (iron) the temperature maximum. Comparing the three cases with the base model, we can see that (1) when the electron temperature is higher, both the carbon and iron charge composition move toward higher charge states, (2) when the electron density is higher, carbon ions move toward higher charge states but iron ions move toward lower charge states, and (3) when the ion velocity is higher, carbon ions move toward lower charge states but iron ions move toward higher charge states. Note that the effects of higher electron density and lower ion velocity are similar, as implied by equation (1). The above results can be understood by considering the shift in the ions' freezing-in region when these physical quantities are changed (compare equations (4)). Therefore to compare the physical conditions in different solar wind source regions where a temperature maximum likely exists, we need the charge composition data of at least two species: one which freezes-in at one side of the temperature maximum (e.g., C) and the other which freezes-in at the other side of the temperature maximum (e.g., Fe). On the basis of our data described in section 4 and the above analysis, we discuss in the following the implied difference in the physical properties among these solar wind source regions.

5.1. Slow Wind and Fast wind

The electron temperature corresponding to the source region of the slow solar wind is higher than that for the fast solar wind from the coronal holes. Note that if the slow solar wind is indeed associated with the streamer region, we expect that the electron density is also higher (and the ion velocity may be slower) than in the coronal hole. Also, the temperature profile of the source region of the slow solar wind may not have a temperature maximum. However, since the freezing-in temperatures of the slow wind are all significantly higher for the four elements, the electron temperature in the slow wind source region is certainly hotter than in the coronal hole region.

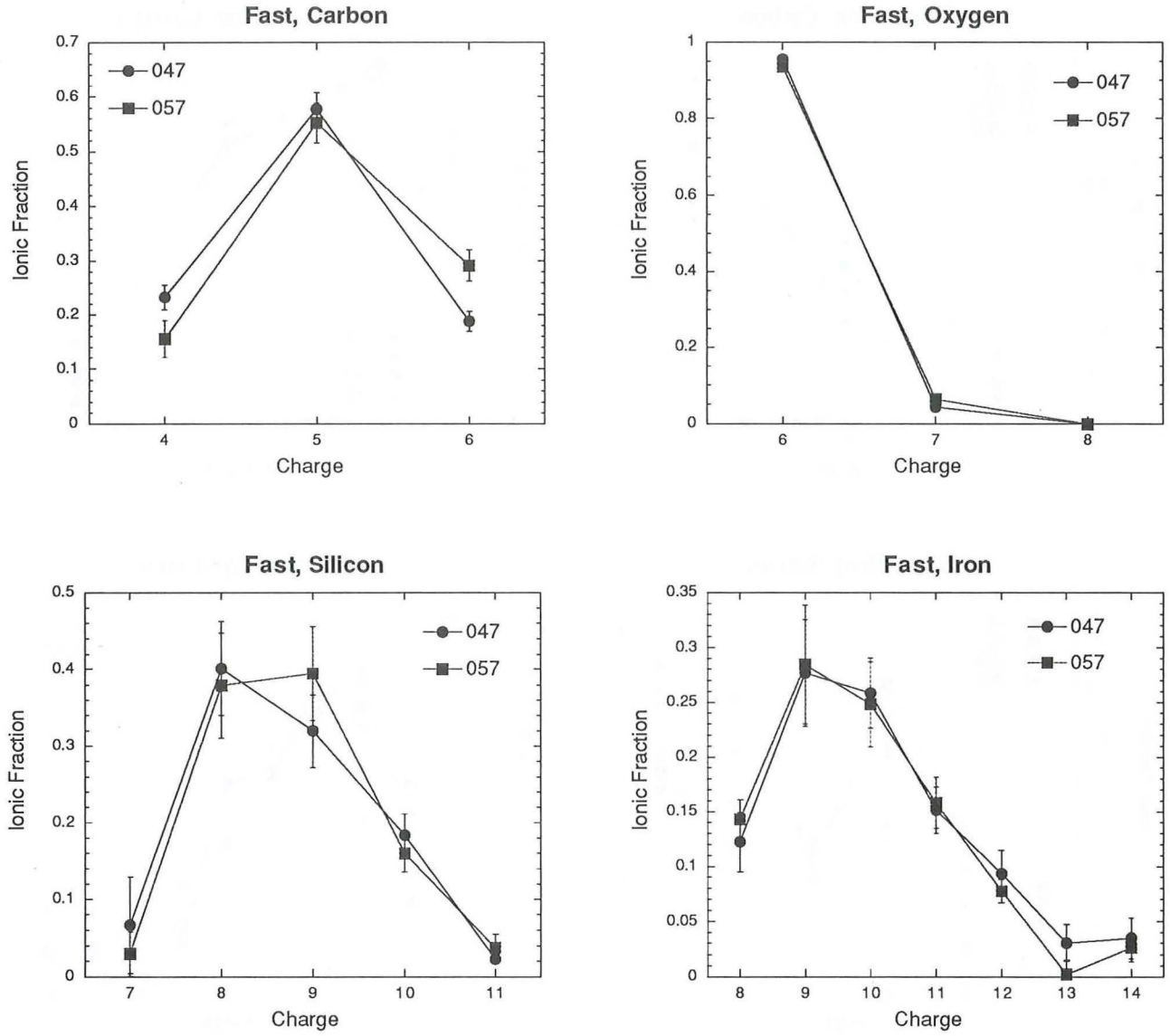

Figure 7. The comparison of the C, O, Si, and Fe charge compositions between the two fast solar wind periods: Fast047 and Fast057.

5.2. North and South Polar Coronal Holes

The electron temperature in the north polar coronal hole seems to be slightly cooler than the south polar coronal hole during this time. One should be aware that both South and North data are for the average fast wind in which the data were integrated through a very long (and different) period of time, thus a large range of heliographic latitudes also. Therefore the difference between the two may be due to time variations or latitudinal variations in the polar holes. *Galvin and Gloeckler* [1998] compared the iron charge composition of the south and north polar holes, both at 70°-80° in situ heliographic latitudes, and found that the north polar coronal hole is cooler than the south polar coronal hole. *Von Steiger* [1998] also showed that the north polar coronal hole is systematically cooler at all in-situ latitudes higher than 40° in the oxygen freezing-in temperature. This would suggest that either there is intrinsic difference in the temperature of the two polar coronal holes, or this difference is caused by time variation. It is worth mentioning that SWOOPS/Ulysses data during the pole-to-pole pass [*Goldstein et al.*, 1996] has also shown a modest north-south high latitude asymmetry. They find that the proton velocity above 40 deg in latitude is on the average 13 to 24 km/s greater at northern latitudes than at southern latitudes and the kinetic temperature is also higher. It suggests the possibility that the electron temperature in the inner corona (as inferred by the ionic charge states data) is correlated with the solar wind speed that higher solar wind speed is related to lower electron temperature in the corona. This may have implications on the coronal heating and solar wind acceleration mechanisms in the inner coronal regions. Further investigation is needed in which one should compare the charge states data from the same latitude of both polar holes and look for the N-S asymmetry.

5.3. Latitudinal Variations in the Polar Coronal Hole

As mentioned in Section 2, several magnetic field models indicate that the footpoints of the solar wind for the Fast data

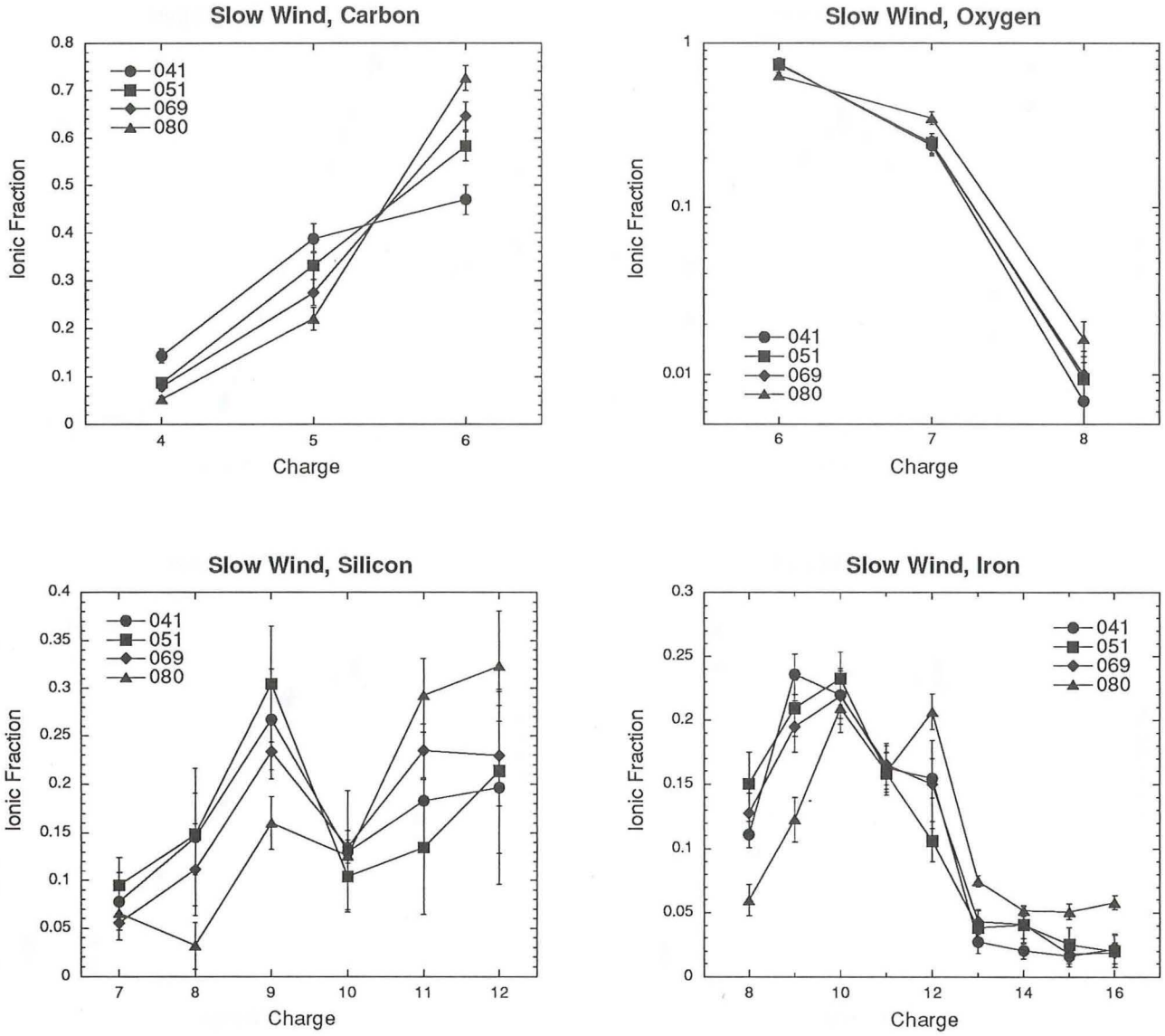

Figure 8. The C, O, Si, and Fe charge compositions of the slow solar wind from the four time periods: Slow041, Slow051, Slow069, Slow080.

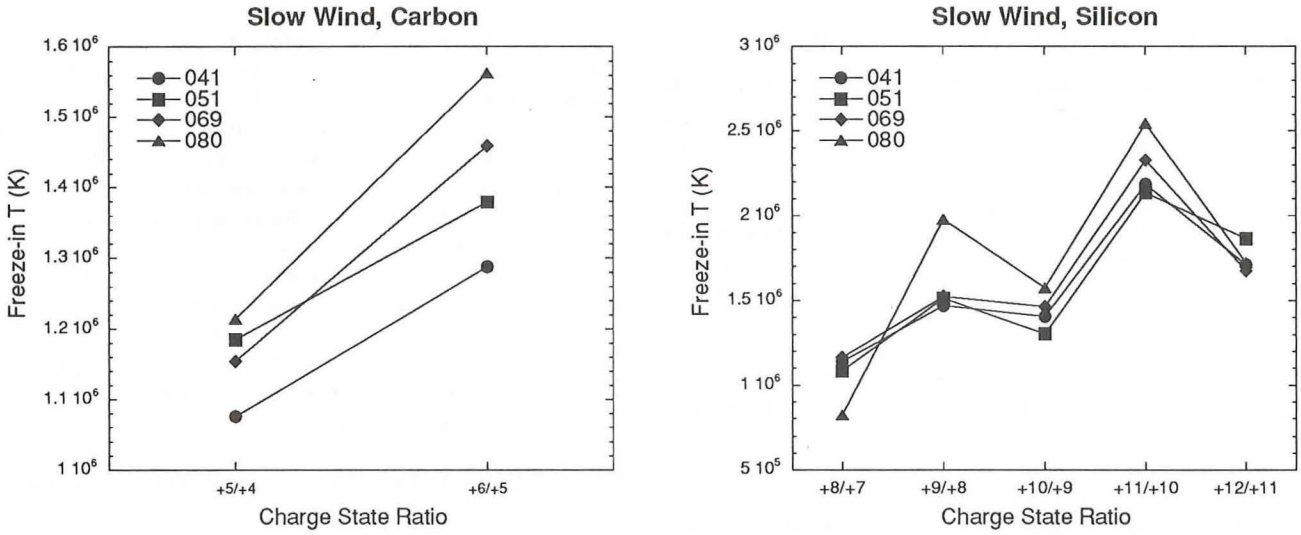

Figure 9. The freezing-in temperature from C and Si ionic ratios of the slow solar wind from the four time periods: Slow041, Slow051, Slow069, Slow080.

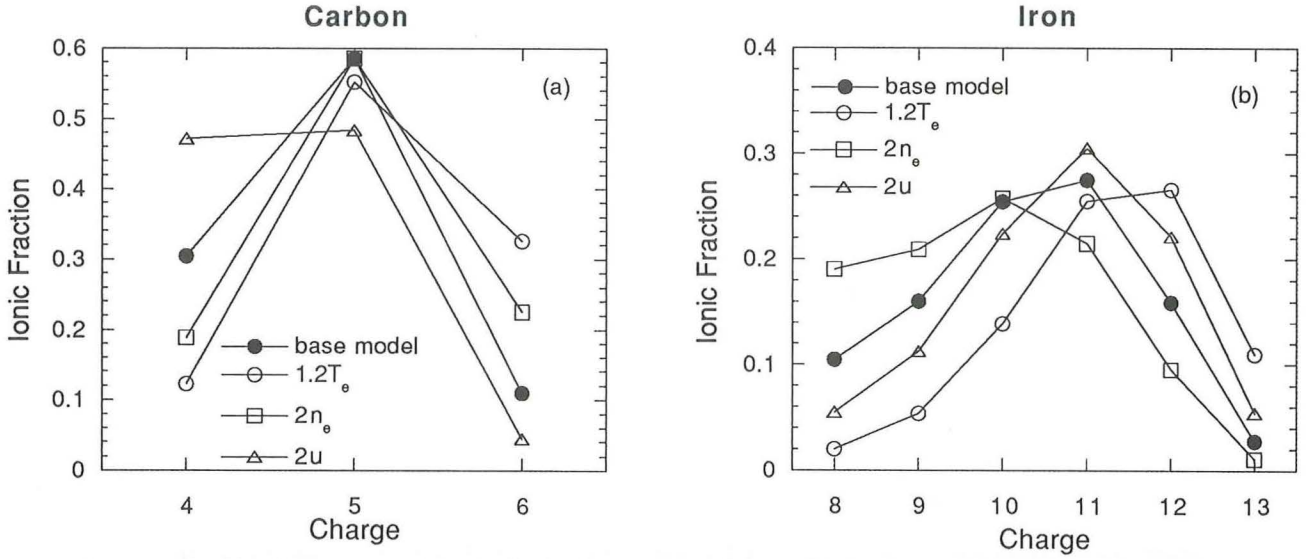

Figure 10. The change in the frozen-in ionic charge states of C and Fe ions compared with the base model ($T_e(r)$, $n_e(r)$ and $u(r)$) (solid circles), when $T_e(r)$ is 1.2 times higher with $n_e(r)$ and $u(r)$ fixed (open circles); or $n_e(r)$ is 2 times higher with $T_e(r)$ and $u(r)$ fixed (open squares); or $u(r)$ is 2 times higher with $T_e(r)$ and $n_e(r)$ fixed (open triangles).

lie near the boundary of the south polar coronal hole, i.e., the lower latitude in the south polar hole. The difference between the Fast and the South data thus implies that there is latitudinal variation in the physical conditions in the polar coronal hole. If we compare with the charge composition data taken from above 70° in situ latitudes of the south polar coronal hole [*Ko et al.*, 1997], we find the same kind of difference. That is, we find a consistent difference in the charge states between the fast wind from high and low latitudes, as those shown in Figure 5. *Galvin and Gloeckler* [1998] have shown that there also exists heliographic latitudinal variations in the Si and Fe ionic charge states in the fast wind from the north polar coronal hole. They move toward higher charge states with higher latitude, which is the same as what we have found in the south polar coronal hole. If we assume the electron temperature does not change along the latitude in the polar coronal hole, this variation in the ionic charge states implies that the electron density is larger or the ion outflow velocity is smaller toward lower latitude (cf. Figures 5 and 10). *Guhathakurta and Holzer* [1994] made coronal white-light observations and found very little intrinsic latitudinal variation in the electron density within the polar coronal hole. On the other hand, *Woo and Habbal* [1997] found from radio occultation measurements that the electron density increases from the high latitude polar coronal hole toward the low latitude streamer belt region. *Strachan et al.* [1998] have shown from UVCS/SOHO (SOHO Ultraviolet Coronagraph Spectrometer) synoptic observation the variation in the O^{+5} outflow velocity as a function of latitude. However, it is not clear if there exists systematic latitudinal dependence of the O^{+5} outflow velocity within the polar coronal hole. Aside from this, there exists no other observation that is capable of deriving outflow velocities of heavy ions. Note that the solar wind proton velocity is smaller in the Fast data than in the South data (cf. Figure 1). This may indicate that the ion velocity is correspondingly smaller in the source region of the Fast data.

Without clear existing observational constraints, we make a simple investigation to find in a quantitative way the possible difference in either the ion velocities or the electron density that may cause the observed differences in the ionic charge state between the Fast and the South data. We do this by finding the change in the ion velocities or electron density that would best fit the data when assuming other physical quantities are kept the same. We start with the South data. We use an electron temperature profile that is one of the best fit temperature profiles for the south polar coronal hole as discussed by *Ko et al.* [1997]. The electron density profile is adopted from the polarization brightness (pB) data observed by the White Light Coronagraph observation on the south polar coronal hole during the SPARTAN 201-1 mission [*Fisher and Guhathakurta*, 1995]. This electron temperature profile and the electron density profile are shown in Figure 11. The ion velocity profile (in km/s) is chosen as a power law in r:

$$u(r) = 699[(r-1)/9]^p + 1. \tag{5}$$

$u(r)$ is defined in such a way that the ion velocity is 1 km/s at 1 solar radii and 700 km/s at 10 solar radii. The power law index p determines how fast the velocity increases from 1 to 10 solar radii. For a given value of p, the frozen-in ionic charge states can be calculated by integrating equation (1). The collisional ionization rates are adopted from *Lennon et al.* [1988] except for iron which are adopted from *Raymond and Smith* [1977]. The autoionization rates are adopted from *Kallman and McCray* [1982]. The radiative and dielectronic recombination rates are adopted from *Arnaud and Raymond* [1992] for iron ions and *Aldrovandi and Pequignot* [1973] for all other ions. Note that these rates are calculated by assuming the electron velocity distribution is thermal (i.e., a Maxwellian). Since the coronal gas is low in density, we also neglect the electron density dependence of the dielectronic recombination rates. The calculated ionic fractions are to be compared with the data using the quantity:

$$\delta_{element,k} \equiv \sum_{i=1}^{I} \left(\frac{y_{k,i,data} - y_{k,i,model}}{\varepsilon_{k,i}} \right)^2 \tag{6}$$

where $y_{k,i,model}$ is the calculated ionic fraction of charge state i

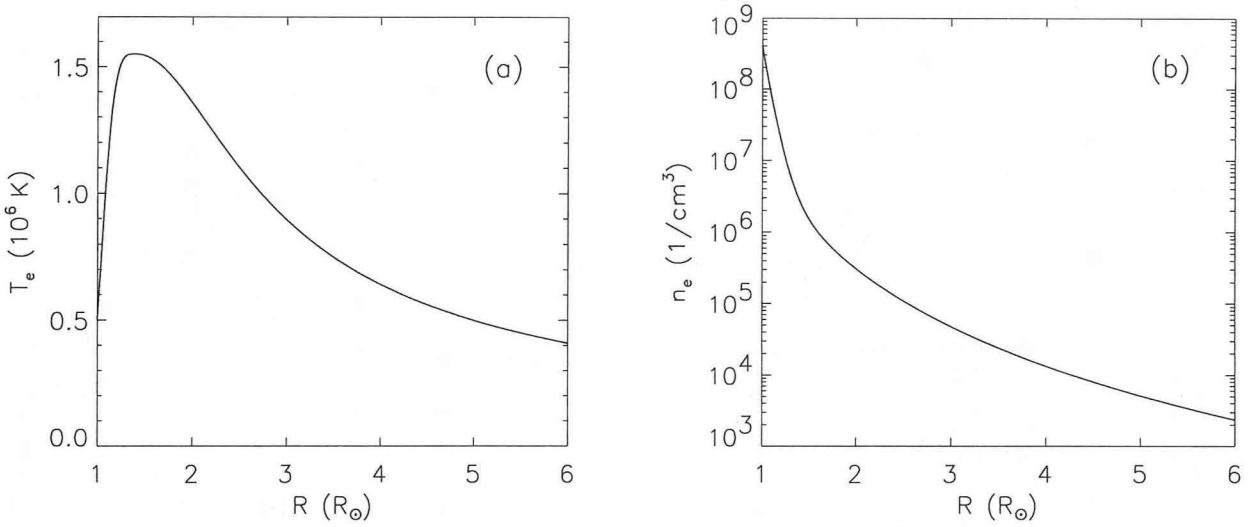

Figure 11. (a) The electron temperature profile and (b) the electron density profile adopted for the south polar coronal hole.

of element k, $y_{k,i,data}$ is the observed ionic fraction, $\varepsilon_{k,i}$ is the error in $y_{k,i,data}$ and l is the number of most abundant ions for a given element included in calculating $\delta_{element,k}$. The ions used in the analysis are C^{+4-+6}, O^{+6-+7}, Si^{+7-+11}, Fe^{+9-+12} (for South data) and Fe^{+8-+12} (for Fast data). The smaller the quantity $\delta_{element,k}$ is, the better the calculated frozen-in ionic fractions of a given element fit with the data.

For each of the four elements, we find the ion velocity (characterized by the value of p) that best fits the data with the adopted electron temperature and density profiles. That is, we find the value of p that minimizes the quantity $\delta_{element,k}$. This is equivalent to the least squares fit of the data to a functional form [*Bevington and Robinson*, 1992] with $\delta_{element,k}$ equivalent to the χ^2 of the fit between the data and the assumed model. However, instead of an explicit function, it is the integration of equation (1) with one free parameter p. Here we assume all ions of the same species flow at the same speed. First we find the ion velocities (i.e., the most probable value of p) that best fit the South data. We then find the ion velocities that best fit the Fast data assuming the same electron temperature and electron density profiles (Figure 11). The difference in the ion velocities is shown in Figure 12. The range of heights that affects the freezing-in process of the ions is shown in solid line (South data) and dashed line (Fast data). This region is defined as from the height where the ionic fractions deviate from their ionization equilibrium values by >10% to the height where the change in the ionic fractions is <1% within 0.1 R_o (thus frozen-in). The regions not relevant in the ion's freezing-in process are drawn in dotted lines. Given that C and O ions freeze-in at 1 to 1.4 R_o (i.e., solar radii), Si ions freeze-in at 1.7 to 2.8 R_o, and Fe ions freeze-in at 2 to 4 R_o (as shown in Figure 12), we find that the ion velocities corresponding to the Fast data is slower than those corresponding to the South data in their respective freezing-in regions by 40--50% for C, O, and Si ions and by 20-30% for Fe ions. This is consistent with the qualitative results discussed above (cf. Figure 10). The different result for Fe from those for other elements may be due to different ranges of Fe charge states used in fitting the data. Note that the oxygen outflow velocity shown here is smaller than that derived from the UVCS/SOHO observation using the Doppler dimming technique on the OVIλ1032/OVIλ1037 line intensity ratios in the polar coronal hole [*Kohl et al.*, 1998; *Cranmer et al.*, 1999]. They showed that the oxygen (O^{+5}) outflow velocity (we will assume all oxygen charge states flow at the same velocity) is ~100 km/s at 1.7 R_o and has reached ~200 km/s at 2 R_o which is much larger than we have shown in Figure 12. Since the ion velocity we discuss here is only relevant in the freezing-in region of the respective ion and O ions are frozen-in very early below 1.4 R_o, it is not clear if the oxygen outflow velocity is also much higher below 1.4 R_o than that shown in Figure 12. If so, the electron temperature profile should be much higher below 1.4 R_o than adopted here (Figure 11a) [*Esser et al.*, 1998]. In any case, the above analysis remains valid in a qualitative sense.

Next we assume that the source region associated with the Fast data has the same electron temperature and ion velocity profiles as those for the South data (see Figures 11a and 12). We then parameterize the electron density profile corresponding to the Fast data as a constant times that for the *South* data (see Figure 11b):

$$n_{e,Fast}(r) = \alpha n_{e,South}(r). \quad (7)$$

Figure 13 shows $\delta_{element,k}$ as a function of α for each element. We find that the best fit electron density (i.e., the value of α that minimizes $\delta_{element,k}$) to the Fast data is for $\alpha \approx 1.5-2.0$. This factor of 1.5-2.0 is consistent with the above analysis for the ion velocities given that higher electron density and lower ion velocity have similar effect on the freezing-in of ions. Si is the only element whose ionic charge states do not show sensitive dependence on α. It is because Si ions have the largest errors in their data and, in this model, freeze-in near the temperature maximum. The change in n_e moves its freezing-in region up and down around the temperature maximum (cf. equation (4)). Therefore the temperature at which Si ions freeze-in, thus its frozen-in charge states, does not vary much. Note that a factor of 2 in electron density is small which may be well within the uncertainties of the coronal pB observations. This small variation, however, leads to non-negligible difference in the observed frozen-in ionic charge states.

Note that the assumed ion velocity (characterized by p) and electron density (characterized by α) profiles in the above analysis do not necessarily represent the "real" condition in

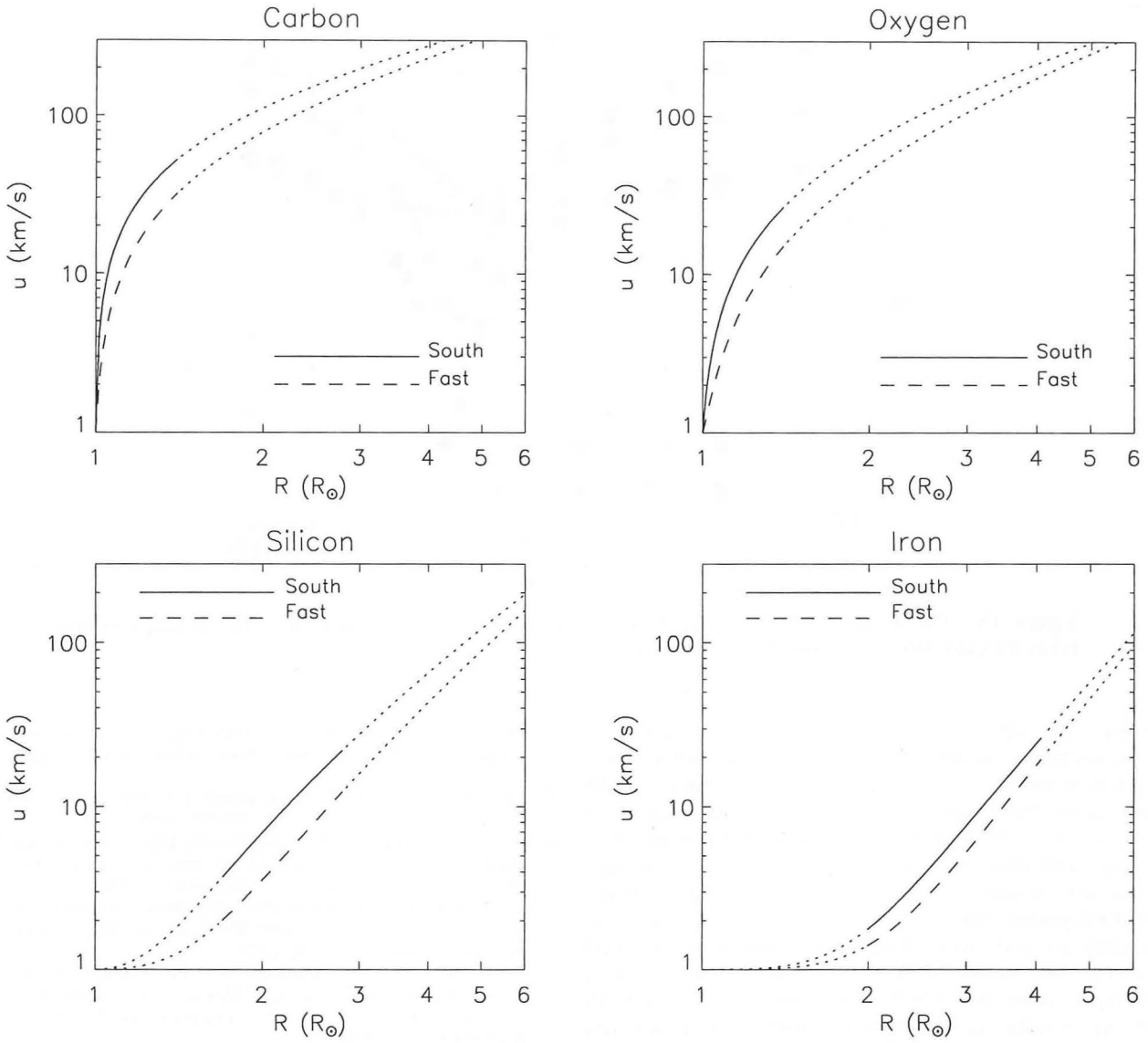

Figure 12. The ion velocities of C, O, Si, and Fe ions that best fit the charge composition data for South compared with those for Fast assuming the electron temperature and electron density profiles are the same in these two regions. The range of heights that affects the freezing-in process of the ions is shown in solid line (South data) and dashed line (Fast data). The regions not relevant in the ion's freezing-in process are drawn in dotted lines.

the polar coronal hole. However, without sufficient observational data to constrain the model, we can at best adopt such forms in our attempt to the quantitative study. It should be emphasized that the three physical quantities that affect the freezing-in process of the ions (i.e., the electron temperature, the electron density and the ion outflow velocity) can all be responsible for the difference in the frozen-in ionic charge states observed along the heliographic latitude. The effect of one of them may just outweigh another. The above "parameter-controlling" analysis merely offers a tool of finding a possible range of the difference in the individual quantity at different latitudes. For example, assuming the electron temperature profile is all the same across the coronal hole, should one find that the electron density at low latitude is four times that at high latitude, the ion velocities at low latitude would then need to be about two times that at high latitude to agree with our observation. This illustrates the clear need to rely on a combined and coordinated data set of the in situ ionic charge states and remote-sensing coronal observations to unambiguously relate the latitudinal variations of these physical quantities to the latitudinal variations of the ionic charge states in the associated solar wind.

6. Summary

We have analyzed the charge composition data observed by SWICS/Ulysses for the slow and fast solar wind during the Ulysses pole-to-pole fast scan in early 1995 and compare these data with those for the fast solar wind from the south and north polar coronal holes. The frozen-in ionic charge states in the slow solar wind indicate that the electron temperature in the source region of the slow solar wind (presumably the streamer region) is, as expected, higher than that in the polar coronal hole. The ionic charge states for the four periods of the slow solar wind analyzed here, however, show non-negligible variations. This indicates the dynamic behavior of

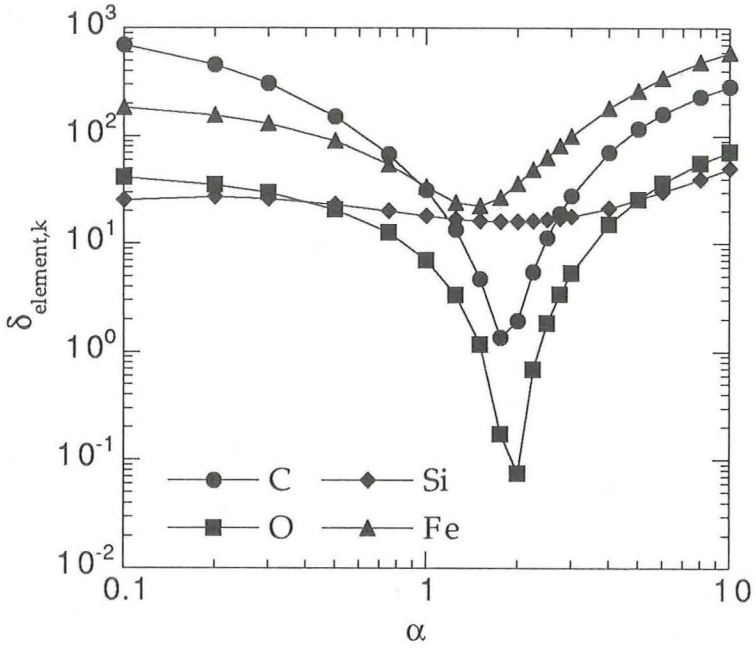

Figure 13. The $\delta_{element,k}$ plotted as a function of α for each element. The smaller the value $\delta_{element,k}$ is, the better the calculated ionic fractions fit with the data.

the physical properties in the source region of the slow solar wind, as opposed to those in the polar coronal hole which is much more stable in this period of the solar minimum. We have shown that the electron temperature in the north polar coronal hole is slightly lower than that in the south polar coronal hole which may be correlated with the north-south asymmetry in the solar wind speed found in the Ulysses SWOOPS plasma experiment data. We have also shown that the difference in the ionic charge states between the fast wind from the lower-latitude coronal hole and the fast wind from an "averaged" polar coronal hole is likely due to either lower ion velocity or higher electron density toward lower latitude, not the electron temperature. A combined data set observed through a coordinated period of time, such as from UVCS/SOHO, white-light coronagraph and radio occultation measurements along with the ionic charge composition data, is needed to understand the difference in the physical properties in the fast wind source regions at different heliographic latitudes.

Acknowledgments. This work is supported by NASA/JPL contract 955460 and NAG 5-2810.

Janet G. Luhmann thanks Rudolf von Steiger and another referee for their assistance in evaluating this paper.

References

Aldrovandi, S. M. V., and D. Pequignot, Radiative and dielectronic recombination coefficients for complex ions, *Astron. Astrophys., 25*, 137-140, 1973.

Arnaud, M., and J. Raymond, Iron ionization and recombination rates and ionization equilibrium, *Astrophys. J., 398*, 394-406, 1992.

Arnaud, M., and R. Rothenflug, An updated evaluation of recombination and ionization rates, *Astron. Astrophys. Suppl. Ser., 60*, 425-457, 1985.

Bevington, P. R., and D. K. Robinson, *Data Reduction and Error Analysis for the Physical Sciences*, 2nd ed., pp. 96-167, McGraw-Hill, New York, 1992.

Cohen, C. M. S., Measurements of solar wind sulfur abundance and charge states, Ph.D. dissertation, Univ. of Maryland, College Park, 1995.

Cranmer, S. R., et al., An empirical model of a polar coronal hole at solar minimum, *Astrophys. J.*, 511, 481-501, 1999.

Esser, R., R. J. Edgar, and N. S. Brickhouse, High minor ion outflow speeds in the inner corona and observed ion charge states in interplanetary space, *Astrophys. J., 498*, 448-457, 1998.

Fisher, R., and M. Guhathakurta, Physical properties of polar coronal rays and holes as observed with SPARTAN 201-01 Coronagraph, *Astrophys. J., 447*, L139-L142, 1995.

Galvin, A. B., Minor ion composition in CME-related solar wind, in *Coronal Mass Ejections*, *Geophys. Monogr. Ser.*, vol. 99, edited by N. Crooker, J. A. Joselyn, and J. Feynman, pp. 253-260, AGU, Washington, D. C., 1997.

Galvin, A. B., and G. Gloeckler, Charge state composition in coronal hole and CME related solar wind: Latitudinal variations observed by Ulysses and WIND, in *Proceedings 31st ESLAB Symposium 'Correlated Phenomena at the Sun in the Heliosphere and in Geospace'*, pp. 323-326, ESA Publications, the Netherlands, 1998.

Geiss, G. et al., The southern high speed stream: Results from SWICS/Ulysses, *Science, 268*, 1033-1036, 1995.

Gloeckler, G., et al., The solar wind ion composition spectrometer, *Astron. Astrophys. Suppl. Ser., 92*, 267-289, 1992.

Goldstein, B. E., et al., Ulysses plasma parameters: Latitudinal, radial, and temporal variations, *Astron. Astrophys., 316*, 296-303, 1996.

Gosling, J. T., P. Riley, D. J. McComas, and V. J. Pizzo, Overexpanding coronal mass ejections at high heliographic latitudes: Observations and simulations, *J. Geophys. Res., 103*, 1941-1954, 1998.

Guhathakurta, M., and T. E. Holzer, Density structure inside a polar coronal hole, *Astrophys. J., 426*, 782-786, 1994.

Hundhausen, A. J., H. E. Gilbert, and S. J. Bame, The state of ionization of oxygen in the solar wind, *Astrophys. J., 152*, L3-L5, 1968.

Kallman, T. R., and R. McCray, X-ray nebular models, *Astrophys. J. Suppl. Ser., 50*, 263-318, 1982.

Ko, Y.-K., L. A. Fisk, G. Gloeckler, and J. Geiss, Limitations on suprathermal tails of electrons in the lower solar corona, *Geophys. Res. Lett., 23*, 2785-2788, 1996.

Ko, Y.-K., L. A. Fisk, J. Geiss, G. Gloeckler, and M. Guhathakurta, An empirical study of the electron temperature and heavy ion velocities in the south polar coronal hole, *Sol. Phys., 171*, 345-361, 1997.

Kohl, J. L., et al., UVCS/SOHO empirical determinations of anisotropic velocity distributions in the solar corona, *Astrophys. J. Lett., 501*, L127-L131, 1998.

Lennon, M. A., et al., Recommended data on the electron impact ionization of atoms and ions: fluorine to nickel, *J. Phys. Chem. Ref. Data, 17*(3), 1285-1363, 1988.

McComas, D. J., et al., Ulysses' return to the slow solar wind, *Geophys. Res. Lett., 25*, 1-4, 1998.

Neugebauer, M., et al., Spatial structure of the solar wind and comparisons with solar data and models, *J. Geophys. Res., 103*, 14587-14599, 1998.

Owocki, S. P., and J. D. Scudder, The effect of a non-Maxwellian electron distribution on oxygen and iron ionization balances in the solar corona, *Astrophys. J., 270*, 758-768, 1983.

Owocki, S. P., and Y.-K. Ko, Charge states of C and O from coronal holes: Non-Maxwellian distribution vs. unequal ion speeds, in *Solar Wind 9*, in press, AIP, New York, 1999.

Phillips, J. L., et al., Ulysses solar wind plasma observations at high southerly latitudes, *Science, 268*, 1030-1033, 1995.

Raymond, J. C., and B. W. Smith, Soft X-ray spectrum of a hot plasma, *Astrophys. J. Suppl. Ser., 35*, 419-439, 1977.

Strachan, L., et al., Determination of 3D coronal structures from UVCS/SOHO synoptic observations, in *Proceedings 31st ESLAB Symposium 'Correlated Phenomena at the Sun in the Heliosphere and in Geospace'*, pp. 539-542, ESA Publications, the Netherlands, 1998.

von Steiger, R., Latitude manifestations of the solar wind, in *Highlights of Astronomy*, *IAU Proceedings*, Kluwer Acad., Norwell, Mass., in press, 1998.

Woo, R., and S. R. Habbal, Extension of coronal structure into interplanetary space, *Geophys. Res. Lett., 24*, 1159-1162, 1997.

C. M. S. Cohen, Space Radiation Laboratory, California Institute of Technology, Pasadena, CA 91125. (email: cohen@srl.caltech.edu)

A. B. Galvin, Institute for the Study of Earth, Oceans, and Space, University of New Hampshire, Durham, NH 03824. (email: GALVIN@celias.sr.unh.edu)

G. Gloeckler, Department of Physics, University of Maryland, College Park, MD 20742. (e-mail: gg10@umail.umd.edu)

Y.-K. Ko, Code 682.3, NASA/GSFC, Greenbelt, MD 20771. (e-mail: kuen@uvcs14.nascom.nasa.gov)

(Received April 6, 1998; revised February 24, 1999;
accepted February 24, 1999.)